Large valley splitting in monolayer WS$_2$ by proximity coupling to an insulating antiferromagnetic substrate

Lei Xu,[1,*] Ming Yang,[2] Lei Shen,[3] Jun Zhou,[1] Tao Zhu,[1] and Yuan Ping Feng[1,4,†]

[1]*Department of Physics, National University of Singapore, Singapore 117542, Singapore*
[2]*Institute of Materials Research and Engineering, A*STAR, 2 Fusionopolis Way, Innovis, Singapore 138634, Singapore*
[3]*Department of Mechanical Engineering, National University of Singapore, Singapore 117575, Singapore*
[4]*Centre for Advanced 2D Materials and Graphene Research Centre, National University of Singapore, Singapore 117546, Singapore*

Lifting the valley degeneracy is an efficient way to achieve valley polarization for further valleytronics operations. In this Rapid Communication, we demonstrate that a large valley splitting can be obtained in monolayer transition metal dichalcogenides by magnetic proximity coupling to an insulating antiferromagnetic substrate. As an example, we perform first-principles calculations to investigate the electronic structures of monolayer WS$_2$ on the MnO(111) surface. Our calculation results suggest that a large valley splitting of 214 meV, which corresponds to a Zeeman magnetic field of 1516 T, is induced in the valence band of monolayer WS$_2$. The magnitude of valley splitting relies on the strength of interfacial orbital hybridization and can be tuned continually by applying an external out-of-plane pressure and in-plane strain. More interestingly, we find that both spin and valley index will flip when the magnetic ordering of MnO is reversed. Besides, owing to the sizable Berry curvature and time-reversal symmetry breaking in the WS$_2$/MnO heterostructure, a spin- and valley-polarized anomalous Hall current can be generated in the presence of an in-plane electric field, which allows one to detect valleys by the electrical approach. Our results shed light on the realization of valleytronic devices using the antiferromagnetic insulator as the substrate.

Introduction. The utilization of valley degree of freedom, which is also called valley pseudospin, as the information carrier is the main context of valleytronics [1–3]. Many systems, such as graphene, silicene, bismuth thin films, and AlAs quantum wells, have been studied to generate, detect, and control the valley pseudospin [3–6]. Valleys, which label the degenerate energy extreme of conduction band or valence band at some special k points, have large separation in the momentum space which enables valley pseudospin very robust against phonon and impurity scatterings. Once the structural inversion symmetry is broken, the carriers at these inequivalent valleys are associated with some valley-contrasting physical quantities, such as Berry curvature Ω and orbital magnetic moment m [2,7]. These distinctive properties make the generation and manipulation of the valley pseudospin accessible by means of electric, magnetic, and optical ways [2,8–14].

Monolayer transition metal dichalcogenides (TMDs) MX_2 ($M =$ Mo, W; $X =$ S, Se, Te) are a class of two-dimensional (2D) materials with direct band gaps, where both conduction band and valence band edges are located at the corners of 2D Brillouin zone. Two inequivalent valleys are formed at K and K' points as a result of the D_{3h} crystal symmetry of pristine monolayer TMDs [15,16], and they constitute a binary index for low-energy carriers [7,17]. Due to the strong spin-orbit coupling (SOC) and intrinsic inversion symmetry

breaking, monolayer TMDs are considered as good candidates for valleytronic applications [3,18,19]. The realization of valley polarization, which breaks the balance of carriers in the inequivalent valleys, is an indispensable step for further manipulation of the valley pseudospin. However, the number of carriers at K and K' valleys is the same as required by the time-reversal symmetry.

Since the orbital magnetic moments in the two valleys are opposite, optical pumping with circularly polarized light has been both theoretically and experimentally demonstrated to be able to achieve valley polarization [9–11]. Nevertheless, as a dynamics process, optical pumping is difficult to manipulate robustly and not applicable for practical valleytronic applications. Interestingly, the valley index and spin index are locked to each other, making it possible to coherently control these two degrees of freedom. Therefore, the magnetic field can be applied to lift the valley degeneracy where spin polarization is accompanied by a valley polarization. Indeed, valley splitting induced by an external magnetic field has been observed in the experiment, whereas the efficiency is very low as 1T magnetic field can only give rise to a splitting of 0.1–0.2 meV [12–14]. On the other hand, some theoretical works reported that doping with transition metal atoms can establish a considerable intrinsic magnetic field in monolayer TMDs, and a large permanent valley polarization will be generated [20,21]. However, these metallic atoms tend to form a cluster and can significantly increase the scattering rate, thus are detriment to the device performance. Moreover, it was predicted that a valley splitting over 300 meV can be generated in monolayer MoTe$_2$ by magnetic proximity coupling to a

---

*xulei0553@gmail.com
†phyfyp@nus.edu.sg

ferromagnetic insulator EuO [22,23]. At the same time, a recent experiment found an enhanced valley splitting in monolayer WSe_2 when deposited on the EuS substrate [24].

In fact, the insulating ferromagnetic materials are very rare and always have a low Curie temperature, but antiferromagnetic insulators are common in nature and easy to be obtained. Hence, it is important and timely to know whether an antiferromagnetic insulator can also induce a valley splitting in monolayer TMDs through magnetic proximity interaction. In this Rapid Communication, we try to answer this question by using first-principles calculations to study valley splitting of the WS_2 monolayer on the antiferromagnetic MnO (111) substrate, due to their small lattice mismatch and the considerable SOC effect in monolayer WS_2. Our calculation results show that the valence band of monolayer WS_2 is well preserved and almost free of hybridization with the substrate, but the conduction band has a strong hybridization with the substrate. Due to the magnetic proximity effect, the valley degeneracy has been lifted, and a sizable valley splitting of 214 meV has been observed in the valence band of monolayer WS_2. The magnitude of splitting can be tuned continually by applying an external pressure and strain. A finite and fully spin- and valley-polarized anomalous Hall conductivity can be obtained when the Fermi level lies between two valley extrema, which makes the WS_2/MnO heterostructure very appealing for both spintronic and valleytronic applications.

Computational details. Our first-principles calculations are performed by using Vienna *ab initio* simulation package (VASP) [25] with generalized gradient approximation (GGA) of Perdew-Burke-Ernzerhof (PBE) functional [26]. The ion-electron interaction is treated by the projector augmented wave method (PAW) [27], and the van der Waals interaction is taken into consideration using the DFT-D3 method [28]. Electron wave function is expanded on a plane-wave basis set with a cut-off energy of 500 eV. A $12 \times 12 \times 1$ Γ-centered Monkhorst-Pack grid is adopted for Brillouin-zone integration. A vacuum slab more than 20 Å is applied along the z direction (normal to the interface) to avoid spurious interaction between repeated slabs. Structural relaxation is carried out using the conjugate-gradient algorithm until the total energy converges to 10^{-5} eV and the Hellmann-Feynman force on each atom is less than 0.01 eV/Å, respectively. In order to include the strong on-site Coulomb interaction in MnO, the Coulomb and exchange parameters U and J are set to 6.9 and 0.86 eV, respectively, for the d orbital of Mn atom [29].

For the calculation of Berry curvature and anomalous Hall conductivity of monolayer WS_2 on the MnO substrate, we employ the maximally localized Wannier function method [30] as implemented in the WANNIER90 package [31]. Ten d orbitals of W atom and six p orbitals of each S atom are selected as the initial orbital projections, and a finer $27 \times 27 \times 1$ uniform k grid is used for the construction of the maximally localized Wannier function. The difference in the spread of total Wannier functions between two successive iterations can converge to 10^{-10} Å^2 within 2000 iterative steps.

Results and discussion. Below the Néel temperature of $T_N = 118$ K, the bulk MnO adopts a rock-salt structure but with rhombohedrally distorted $B1$ symmetry [32]. The optimized lattice constant of bulk MnO is 4.53 Å, which is

close to the experimental measurement value of 4.44 Å [33]. Besides, our DFT $+ U$ calculations also predict that bulk MnO is a type-II antiferromagnetic insulator with a band gap of 2.1 eV and the magnetic ordering along (111) direction. The calculated magnetic moment on each Mn atom is $4.66\mu_B$, which is in good agreement with the experimental result of $4.58\mu_B$ [34]. Based on the optimized structures, the MnO (111) slab and monolayer WS_2 have in-plane lattice constants of 3.203 and 3.184 Å, respectively, with a lattice mismatch of 0.6%. We fix the in-plane lattice constant of the WS_2/MnO heterostructure to the value of MnO (111) slab, thus a small tensile strain is applied in monolayer WS_2. The substrate is constructed by six bilayers of MnO, and the bottom layer is always terminated by O atoms which are passivated with hydrogen atoms to avoid surface states.

There are two possible top surface terminations of the MnO (111) substrate; one is terminated by Mn atoms, and the other is terminated by O atoms. The binding energy, which is defined as the energy difference between the WS_2/MnO heterostructure and the isolated systems, for the Mn-terminated top surface is calculated to be 0.33 eV larger than that of the O-terminated top surface. It indicates that Mn-terminated substrate has a much stronger interaction with monolayer WS_2. Besides, monolayer WS_2 is much closer to the magnetic Mn atoms in the Mn-terminated case, so the magnetic proximity effect is expected to be more significant. Therefore, we will focus on monolayer WS_2 on the Mn-terminated MnO (111) surface in the following discussion. For the interfacial configurations, we have investigated six possible constructions by considering high symmetrical positions, namely, the topmost Mn atom or O atom in the substrate directly below W atom, S atom, or hexagonal hollow site of monolayer WS_2. Among these six configurations, the one with the topmost Mn atom directly below the W atom and the topmost O atom sits below the hexagonal hollow site is the most stable one, as shown in Fig. 1. The separation between surface Mn atoms and W atoms, which is defined as interfacial distance d, is calculated to be 3.645 Å, and such a short distance implies that the MnO substrate
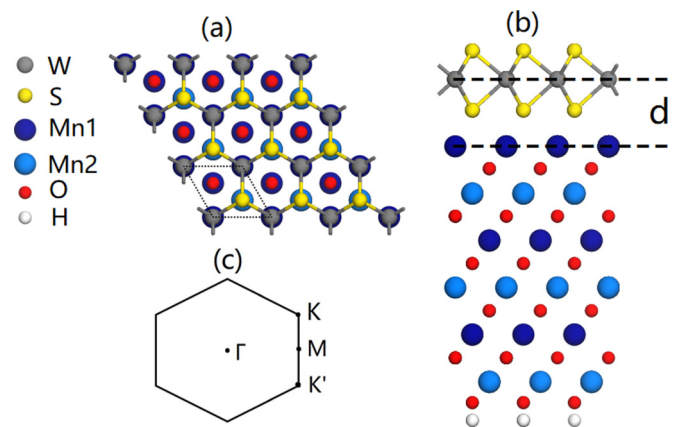

FIG. 1. (a) Top view and (b) side view of the WS_2/MnO heterstructure, Mn1 and Mn2 represent the Mn atoms with opposite spin polarizations. The defined interface distance is denoted by d. (c) The first Brillouin zone of the WS_2/MnO structure with high-symmetry points, and the primitive unit cell is shown by dotted lines in (a).
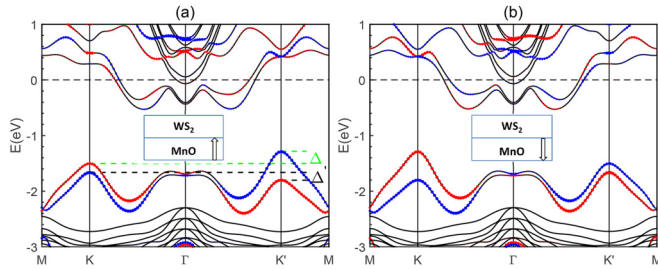
FIG. 2. (a) and (b) The band structure of the WS$_2$/MnO heterostructure with SOC for surface Mn(Mn1) atoms magnetized upward and downward, respectively, the spin projections for monolayer WS$_2$ states along the positive (spin-up) and negative (spin-down) z axes are denoted by blue and red weighted solid circles, respectively. The magnitudes of the valley splitting in the first and second valence bands are denoted by Δ and Δ' in (a). The empty arrow in the inset shows the direction of the surface Mn(Mn1) atoms' magnetic ordering.

FIG. 3. Spin-polarized partial density of states of the WS$_2$/MnO heterostructure, and the Fermi level is set to 0.

would cause important impacts on the monolayer WS$_2$. Indeed, we find a magnetic moment of $0.05\mu_B$ has been induced on the W atom, and at the same time, the top and bottom S atoms acquire a magnetic moment of 0.01 and $0.02\mu_B$, respectively. It is noted that these magnetic moments are all ferromagnetically coupled with the interfacial Mn(Mn1) atom. The induced magnetism will break the time-reversal symmetry of monolayer WS$_2$, and we expect the valley degeneracy should be lifted simultaneously.

In Fig. 2(a), we show the band structure of the WS$_2$/MnO heterostructure with SOC and surface Mn(Mn1) atoms magnetized upward. The spin projections for monolayer WS$_2$ states along the positive (spin-up) and negative (spin-down) z directions are indicated by blue and red weighted solid circles, respectively. As can be seen, the conduction band of monolayer WS$_2$ has a strong orbital hybridization with the substrate, and its valley characteristic has been partly destroyed. Based on Bader analysis [35], we find that an amount of $0.49e^-$ is transferred from the substrate to the monolayer WS$_2$. Consequently, the Fermi level is shifted into the conduction band. In contrast, the valence band of monolayer WS$_2$ is little affected by the substrate, and the two valleys (K and K') are well preserved. The spin-polarized density of states (SOC not included), as shown in Fig. 3, also illustrates that the conduction band edge states are contributed by both WS$_2$ and MnO, whereas the valence band edge states are only originated from WS$_2$ orbitals. In addition, we note that there is an energy shift of around 177 meV between the valence band maxima of the two spin channels, which is resulted from the substrate induced magnetism in monolayer WS$_2$.

For freestanding monolayer WS$_2$, there is a large spin splitting in both K and K' valleys due to the inversion symmetry breaking and strong SOC, while the spin-up band in one valley is energy degenerate with the spin-down band in the other valley as a result of time-reversal symmetry [7]. However, as shown in Fig. 2(a), the valley degeneracy in monolayer WS$_2$ has been lifted when placed onto the MnO substrate. Here, we only consider the valleys in the valence band of monolayer WS$_2$, and we define the valley splitting Δ as the
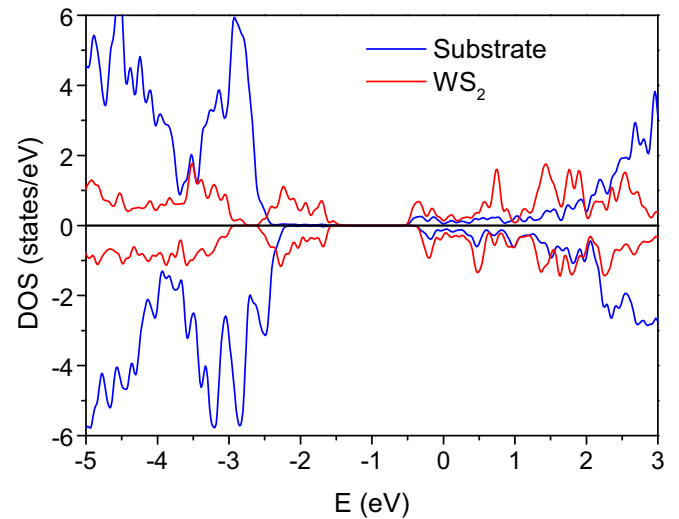
energy difference between the two valley extrema as denoted in Fig. 2(a). Within this definition, the valley splitting in the valence band of monolayer WS$_2$ is found to be 214 meV, which is sizable and comparable to the valley splittings predicted from the MoTe$_2$/EuO and MoS$_2$/EuS heterostructures [22,23,36]. Besides, we also calculate the band structures of the other five possible configurations (see the Supplemental Material [37]) and find that the valley splittings for different interface configurations vary from 63 to 289 meV, which indicates that the proximity effect induced valley splitting is very robust.

The magnetic proximity effect induced valley splitting is mediated with the interfacial orbital hybridization between monolayer WS$_2$ and MnO, and we expect its magnitude can be modulated by changing the hybridization strength. In the experiment, one can apply an external perpendicular pressure or insert a buffer layer into the heterostructure to adjust the interface distance, and then the interfacial orbital hybridization will be altered [38–40]. Figure 4(a) shows the variation of valley splitting as a function of interface distance. It can be seen that the splitting is very sensitive to the separation, for example, the valley splitting can reach a value over 0.4 eV for a slightly smaller distance of 3.3 Å but almost vanishes when the separation is larger than 5.5 Å, which implies that the magnetic proximity coupling is a short-range effect. On the other hand, the strain effect also has an important influence on the band hybridization. By calculating the band structures of the WS$_2$/MnO heterostructure under different in-plane strains, we find that the valley splitting also has a strong dependence on the applied external strain. As shown in Fig. 4(b), a compressive strain can increase the valley splitting due to the enhanced hybridization, whereas a tensile strain will decrease the valley splitting. Hence, we can continually tune the magnitude of valley splitting by external pressure and strain methods.

In order to have a better understanding of the magnetic proximity interaction induced large valley splitting, we construct a low-energy effective Hamiltonian based on the $k \cdot p$ model
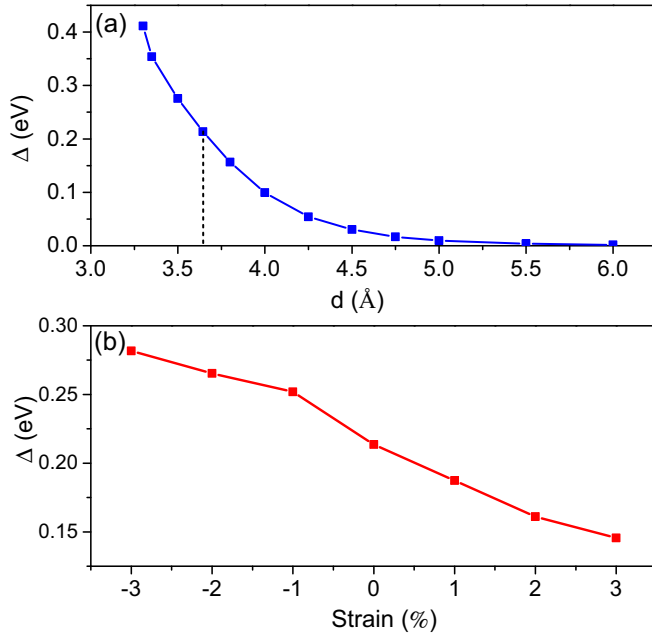
FIG. 4. Valley splitting Δ as a function of (a) the interfacial distance d where the equilibrium distance is denoted by the dashed line, and (b) the in-plane strain.

FIG. 5. Calculated Berry curvature of monolayer WS$_2$ on the MnO substrate (a) over 2D Brillouin zone and (b) along high-symmetry lines. (c) The calculated intrinsic anomalous Hall conductivity σ_{xy} as a function of Fermi energy, and the two dashed lines denote the two valley extrema.

[17]. The Hamiltonian is expressed as

$$H = at(\tau k_x \hat{\sigma}_x + k_y \hat{\sigma}_y) + \frac{\Delta}{2} \hat{\sigma}_z - \lambda \tau \frac{\hat{\sigma}_z - 1}{2} \hat{s}_z$$
$$+ \frac{\hat{\sigma}_z - 1}{2} (\hat{s}_z + \tau \alpha) B, \quad (1)$$

where a, t, Δ, 2λ, α, and B are the lattice constant, effective hopping parameter, band gap, SOC strength, orbital magnetic moment, and effective Zeeman magnetic field, respectively. $\hat{\sigma}$ is the Pauli spin matrix which is constructed on the bases $|d_{z^2}\rangle$ and $\frac{1}{\sqrt{2}}(|d_{x^2-y^2}\rangle + i\tau|d_{xy}\rangle)$. Besides, $\tau = \pm 1$ and $\hat{s}_z = \pm 1$ are the valley index and spin index, respectively. The first three terms of the Hamiltonian describe the low-energy band dispersion of pristine monolayer WS$_2$, while the last term accounts for the proximity induced exchange energy. It should be emphasized that the spin and valley degeneracies are still remained in the conduction band but lifted in the valence band for this Hamiltonian.

It can be found that the presence of the antiferromagnetic substrate MnO introduces a Zeeman magnetic field B, which lifts the valley degeneracy by coupling to the orbital and spin magnetic moment in the monolayer WS$_2$. Based on the eigenvalues of the Hamiltonian, we can deduce that the valley splitting Δ is $2(1 + \alpha)B$. To determine the value of B, we introduce another valley splitting $\Delta' = 2(1 - \alpha)B$, which is the splitting of the second valence band, as shown in Fig. 2(a). By fitting the two valley splittings with the first-principles calculation results ($\Delta = 214$ and $\Delta' = 137$ meV), an orbital magnetic moment α of 0.22 [41] and an effective Zeeman field B of 87.75 meV can be obtained. The substrate induced effective Zeeman field corresponds to an equivalent magnetic field of 1516 T, which indicates a huge perpendicular magnetic
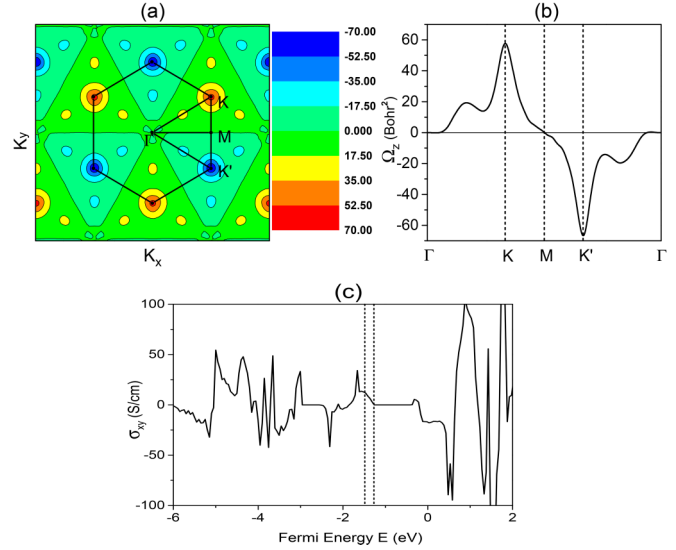
field is built into the monolayer WS$_2$ through the magnetic proximity interaction.

When we tune the Fermi level to the energy window between two valley extrema by a gate voltage or hole doping the WS$_2$/MnO heterostructure, both spin and valley polarizations will be achieved. More interestingly, we find that both spin and valley indices of the transport carriers can be flipped when reversing the magnetic ordering of MnO, as shown in Figs. 2(a) and 2(b). In experiment, one can deposit MnO onto a hard magnetic material (such as FePt or CoPt), which can not only pin the MnO's magnetic ordering, but also help to flip it in the presence of an external magnetic field.

Due to the intrinsic inversion symmetry breaking in monolayer WS$_2$, the charge carriers in the K and K' valleys will acquire a nonzero Berry curvature Ω along the out-of-plane direction (z axis). As derived from the Kudo formula [42,43], the Berry curvature can be written as a summation of all occupied contributions,

$$\Omega(k) = - \sum_n \sum_{n \neq n'} f_n \frac{2\, \text{Im}\langle \psi_{nk} | v_x | \psi_{n'k} \rangle \langle \psi_{n'k} | v_y | \psi_{nk} \rangle}{(E_n - E_{n'})^2}, \quad (2)$$

where f_n is the Fermi-Dirac distribution function and $v_{x(y)}$ is the velocity operator. $|\psi_{nk}\rangle$ is the Bloch wave function with eigenvalue E_n. In Figs. 5(a) and 5(b), we show the calculated Berry curvature in the 2D Brillouin zone and along the high-symmetry lines, where the Fermi level has already been shifted into the WS$_2$ band gap. Obviously, the Berry curvature is sizable and takes opposite signs in the vicinity of K and K' valleys, which reveal that the valley-contrasting characteristic is still remained in monolayer WS$_2$ even strongly hybridized with the MnO substrate. Under an in-plane longitudinal electric field, the Berry curvature will give rise to an anomalous transverse velocity $v_\perp$ for Bloch electrons, $v_\perp \sim E \times \Omega(k)$ [1]. Thus, charge carriers in the K and K' valleys will move
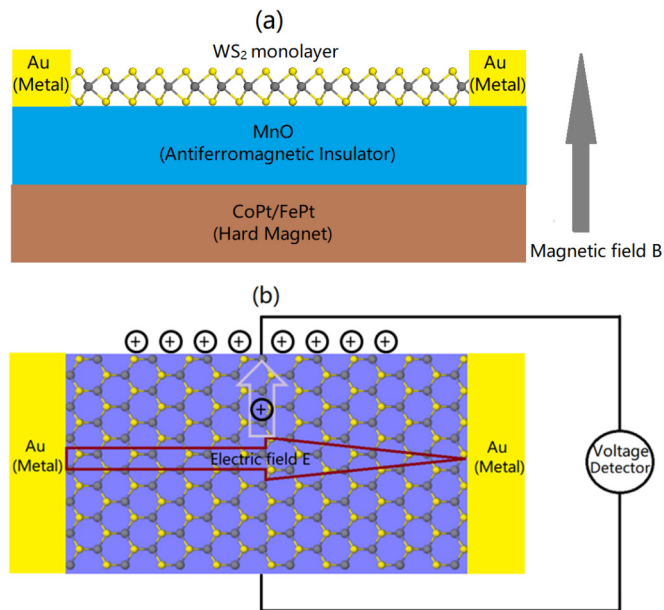
FIG. 6. (a) Top view and (b) side view of the proposed valleytronic device.

in opposite directions due to the valley-contrasting Berry curvature.

Owing to the giant valley splitting and sizable Berry curvature in the monolayer WS$_2$, an anomalous Hall current would be observed when an in-plane electric field is applied to the WS$_2$/MnO heterostructure. By integrating the Berry curvature over the 2D Brillouin zone, we can obtain the intrinsic anomalous Hall conductivity σ_{xy} [1,42]. In Fig. 5(c), we show the calculated σ_{xy} as a function of Fermi energy. As can be seen, when the Fermi level lies between the valence band maxima of the K and K' valleys, as denoted by the dashed lines, a fully spin- and valley-polarized Hall conductivity will be generated. This provides us with a method to detect the valley pseudospin by electric measurement and forms the basis for the application of the valleytronic device. In Fig. 6, we propose a device to experimentally investigate the valley anomalous Hall effect, where the antiferromagnetic insulator is not only severed as a substrate, but also to achieve valley polarization

in its supported monolayer WS$_2$. Besides, a hard magnet is used to pin the magnetic ordering of the antiferromagnetic insulator. When hole doping the system to enable the Fermi level lies between the two valleys, the transport carriers, i.e., spin-up holes from the K' valley [Fig. 2(a)], will move toward the upside in the presence of an in-plane external electric field due to their negative Berry curvatures, as shown in Fig. 6(b). The accumulated holes will result in a net measurable voltage along the transversal direction, which can be detected experimentally by a voltmeter. Once the magnetic ordering of the MnO substrate is reversed by an external magnetic field, spin-down holes from the K valley [Fig. 2(b)] will act as free carriers and move toward the downside since they have positive Berry curvatures, and then a voltage with opposite sign will be detected. It should be noted that the transport carriers have particular polarity for charge, spin, and valley, and the anomalous Hall current is a combination of all three of them.

Conclusion. To summarize, through the magnetic proximity coupling to the insulating antiferromagnetic MnO substrate, a large valley splitting of 214 meV is induced in the valence band of monolayer WS$_2$ based on our first-principles calculations. The magnetic proximity interaction is mediated with interfacial orbital hybridization, and as a result the induced valley splitting shows a strong dependence on the interface distance and strain. Besides, the sizable and valley-contrasting Berry curvature still remained in monolayer WS$_2$ despite its strong interaction with the MnO substrate. Due to the large valley splitting and time-reversal symmetry broken in the WS$_2$/MnO heterostructure, a finite and fully spin- and valley-polarized anomalous Hall conductivity can be obtained when the Fermi level is shifted between the maxima of the two valleys. Therefore, the WS$_2$/MnO heterostructure provides a good platform to detect the valley pseudospin and study the anomalous Hall effect. These findings are also expected to be applicable to other valley materials coupling to insulating antiferromagnetic substrates.

[1] D. Xiao, M.-C. Chang, and Q. Niu, Rev. Mod. Phys. **82**, 1959 (2010).

[2] D. Xiao, W. Yao, and Q. Niu, Phys. Rev. Lett. **99**, 236809 (2007).

[3] J. R. Schaibley, H. Yu, G. Clark, P. Rivera, J. S. Ross, K. L. Seyler, W. Yao, and X. Xu, Nat. Rev. Mater. **1**, 16055 (2016).

[4] A. Rycerz, J. Tworzydlo, and C. W. J. Beenakker, Nat. Phys. **3**, 172 (2007).

[5] M. Ezawa, Phys. Rev. B **87**, 155415 (2013).

[6] Z. Zhu, A. Collaudin, B. Fauque, W. Kang, and K. Behnia, Nat. Phys. **8**, 89 (2012).

[7] W. Feng, Y. Yao, W. Zhu, J. Zhou, W. Yao, and D. Xiao, Phys. Rev. B **86**, 165108 (2012).

[8] W. Yao, D. Xiao, and Q. Niu, Phys. Rev. B **77**, 235406 (2008).

[9] H. Zeng, J. Dai, W. Yao, D. Xiao, and X. Cui, Nat. Nanotechnol. **7**, 490 (2012).

[10] T. Cao, G. Wang, W. Han, H. Ye, C. Zhu, J. Shi, Q. Niu, P. Tan, E. Wang, B. Liu, and J. Feng, Nat. Commun. **3**, 887 (2012).

[11] K. F. Mak, K. He, J. Shan, and T. F. Heinz, Nat. Nanotechnol. **7**, 494 (2012).

[12] G. Aivazian, Z. Gong, A. M. Jones, R.-L. Chu, J. Yan, D. G. Mandrus, C. Zhang, D. Cobden, W. Yao, and X. Xu, Nat. Phys. **11**, 148 (2015).

[13] D. MacNeill, C. Heikes, K. F. Mak, Z. Anderson, A. Kormányos, V. Zólyomi, J. Park, and D. C. Ralph, Phys. Rev. Lett. **114**, 037401 (2015).

[14] Y. Li, J. Ludwig, T. Low, A. Chernikov, X. Cui, G. Arefe, Y. D. Kim, A. M. van der Zande, A. Rigosi, H. M. Hill, S. H. Kim, J. Hone, Z. Li, D. Smirnov, and T. F. Heinz, Phys. Rev. Lett. **113**, 266804 (2014).

[15] A. Kormányos, V. Zólyomi, N. D. Drummond, P. Rakyta, G. Burkard, and V. I. Fal'ko, Phys. Rev. B **88**, 045416 (2013).

[16] A. Kormányos, G. Burkard, M. Gmitra, J. Fabian, V. Zólyomi, N. D. Drummond, and V. Falko, 2D Mater. **2**, 022001 (2015).

[17] D. Xiao, G.-B. Liu, W. Feng, X. Xu, and W. Yao, Phys. Rev. Lett. **108**, 196802 (2012).

[18] G.-B. Liu, D. Xiao, Y. Yao, X. Xu, and W. Yao, Chem. Soc. Rev. **44**, 2643 (2015).

[19] X. Xu, W. Yao, D. Xiao, and T. F. Heinz, Nat. Phys. **10**, 343 (2014).

[20] N. Singh and U. Schwingenschlögl, Adv. Mater. **29**, 1600970 (2017).

[21] Y. Cheng, Q. Zhang, and U. Schwingenschlögl, Phys. Rev. B **89**, 155429 (2014).

[22] Q. Zhang, S. A. Yang, W. Mi, Y. Cheng, and U. Schwingenschlögl, Adv. Mater. **28**, 959 (2016).

[23] J. Qi, X. Li, Q. Niu, and J. Feng, Phys. Rev. B **92**, 121403 (2015).

[24] C. Zhao, T. Norden, P. Zhang, P. Zhao, Y. Cheng, F. Sun, J. P. Parry, P. Taheri, J. Wang, Y. Yang, T. Scrace, K. Kang, S. Yang, G.-x. Miao, R. Sabirianov, G. Kioseoglou, W. Huang, A. Petrou, and H. Zeng, Nat. Nanotechnol. **12**, 757 (2017).

[25] G. Kresse and J. Furthmüller, Phys. Rev. B **54**, 11169 (1996).

[26] J. P. Perdew, K. Burke, and M. Ernzerhof, Phys. Rev. Lett. **77**, 3865 (1996).

[27] P. E. Blöchl, Phys. Rev. B **50**, 17953 (1994).

[28] S. Grimme, J. Antony, S. Ehrlich, and H. Krieg, J. Chem. Phys. **132**, 154104 (2010).

[29] V. I. Anisimov, J. Zaanen, and O. K. Andersen, Phys. Rev. B **44**, 943 (1991).

[30] N. Marzari, A. A. Mostofi, J. R. Yates, I. Souza, and D. Vanderbilt, Rev. Mod. Phys. **84**, 1419 (2012).

[31] A. A. Mostofi, J. R. Yates, Y.-S. Lee, I. Souza, D. Vanderbilt, and N. Marzari, Comput. Phys. Commun. **178**, 685 (2008).

[32] H. Shaked, J. Faber, and R. L. Hitterman, Phys. Rev. B **38**, 11901 (1988).

[33] R. Wyckoff, *Crystal Structures* (Interscience, New York, 1964), Vol. 2.

[34] B. E. F. Fender, A. J. Jacobson, and F. A. Wedgwood, J. Chem. Phys. **48**, 990 (1968).

[35] G. Henkelman, A. Arnaldsson, and H. Jónsson, Comput. Mater. Sci. **36**, 354 (2006).

[36] X. Liang, L. Deng, F. Huang, T. Tang, C. Wang, Y. Zhu, J. Qin, Y. Zhang, B. Peng, and L. Bi, Nanoscale **9**, 9502 (2017).

[37] See Supplemental Material at http://link.aps.org/supplemental/10.1103/PhysRevB.97.041405 for different interfacial configurations and the corresponding band structures.

[38] Z. Zhao, H. Zhang, H. Yuan, S. Wang, Y. Lin, Q. Zeng, G. Xu, Z. Liu, G. Solanki, K. Patel *et al.*, Nat. Commun. **6**, 7312 (2015).

[39] A. P. Nayak, S. Bhattacharyya, J. Zhu, J. Liu, X. Wu, T. Pandey, C. Jin, A. K. Singh, D. Akinwande, and J.-F. Lin, Nat. Commun. **5**, 3731 (2014).

[40] M. Farmanbar and G. Brocks, Phys. Rev. B **91**, 161304 (2015).

[41] Here, in order to keep the same with $\hat{s}_z$, α is unitless, and we place its unit μ_B into Zeeman field B.

[42] Y. Yao, L. Kleinman, A. H. MacDonald, J. Sinova, T. Jungwirth, D.-s. Wang, E. Wang, and Q. Niu, Phys. Rev. Lett. **92**, 037204 (2004).

[43] D. J. Thouless, M. Kohmoto, M. P. Nightingale, and M. den Nijs, Phys. Rev. Lett. **49**, 405 (1982).